POLYOXOMETALATES

Open Access
RESEARCH ARTICLE

Ligand functionalization of mononuclear Pt-polyoxometalate for enhanced hydrogen evolution reaction activity

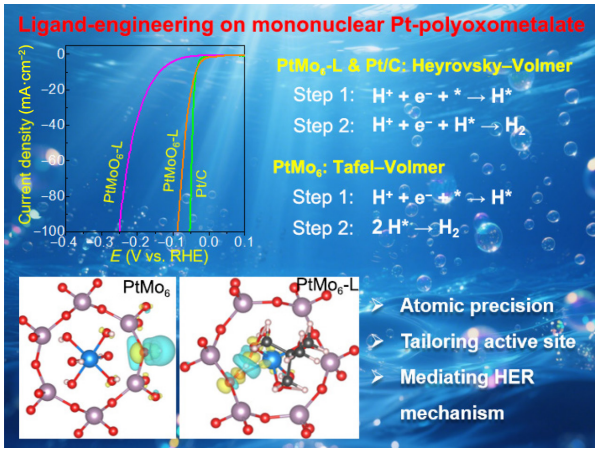
Zhaoxian Qin[§], Chenglong Chi[§], Huan Li, Wei Jian✉, Jingjing Zhang, and Gao Li✉

School of Chemistry and Chemical Engineering, Inner Mongolia Normal University, Hohhot 010022, China
[§]Zhaoxian Qin and Chenglong Chi contributed equally to this work.

Cite This: *Polyoxometalates*, **2026**, *5*, 9140144

Read Online

ABSTRACT: Hydrogen evolution reaction (HER) in electrocatalytic water splitting for producing green hydrogen has recently emerged as a promising approach to address the current energy and environmental challenges. In this study, we prepared and characterized the mononuclear Pt-polyoxometalate clusters $[Pt_1Mo_6(OH)_6O_{18}](NH_4)_2$ ($PtMo_6$) and $[Pt_1Mo_6(OH)_3O_{18})O_3C_5H_9]TBA_2$ ($PtMo_6$-L, TBA: tetrabutylammonium) as HER electrocatalysts with enhanced activity. The HER performance of $PtMo_6$-L coated onto glassy carbon is superior to that of naked $PtMo_6$ and comparable to that of commercial 20 wt.% Pt/C, with an overpotential of 37 mV@10 $mA{\cdot}cm^{-2}$ and a Tafel slope of 42 $mV{\cdot}dec^{-1}$. The HER follows the Heyrovsky–Volmer mechanism over $PtMo_6$-L, similar to Pt/C, but the Tafel–Volmer mechanism over $PtMo_6$. Experimental and density functional theory calculation results indicate that the Pt–O–H group in the polyoxometalate clusters is the active site for the HER. Moreover, mechanistic studies reveal that the negatively charged C_5H_9-bonded O1 in $PtMo_6$-L is prone to proton adsorption and activation, thereby enhancing electrocatalytic HER activity. Overall, this study provides new insights into the polyoxometalate structure–electrocatalytic property relationship at the precise atomic and molecular levels, advancing HER research.



KEYWORDS: polyoxometalates, atomically precise $PtMo_6$, electrocatalytic water splitting, hydrogen evolution reaction, computational study

1 Introduction

Pt-based materials are considered state-of-the-art electrocatalysts for the hydrogen evolution reaction (HER) because their extremely low overpotential for the HER overcomes its high energy barrier and fast kinetics [1–7]. Recently, extensive research efforts have been devoted to designing new types of Pt-based electrocatalysts using composition-, morphology-, and crystal-phase-engineering strategies. In particular, to boost the utilization and catalytic efficiency of Pt in the HER, single-atom catalysts (SACs) have attracted intense attention [8–15]. However, the effect of the location and coordination environment of single-atom Pt on the reaction pathway and activation energy is unpredictable. In addition, stabilizing isolated Pt atoms on appropriate supports with high metal loading without compromising catalytic activity and product selectivity remains a challenge that hinders the practical applications of Pt SACs.

In this context, we envisaged that polyoxometalates containing single-atom Pt [16] could serve as a readily available and ideal Pt SAC model to study the electrocatalytic HER owing to the following advantages: (i) Polyoxometalates are a unique type of nanoscale early transition-metal-oxo clusters with definite structures and superior physical and electrochemical properties [17–23]. The unique structural versatility of polyoxometalates in terms of composition, structure, and coordination environment provides an ideal platform to investigate the structure–activity relationship in SACs [24]. (ii) The excellent catalytic redox activity of polyoxometalates allows them to effectively undergo multielectron redox transformations without any structural alteration [25–27]. (iii) Polyoxometalates also serve as support materials for SACs. For example, phosphomolybdic acid effectively stabilizes single-atom Pt with a high loading (> 10 wt.%) [28–30]. In Pt-doped polyoxometalates, the Pt–O bonds accelerate the coupling of protons and electrons for the rapid release of hydrogen [31]. However, the specific roles of the Pt–O and Pt–O–H bonds in polyoxometalates during the HER remain unclear.

Received: February 9, 2026; **Revised:** June 18, 2026
Accepted: June 22, 2026

✉Address correspondence to Wei Jian, jianwei@imnu.edu.cn; Gao Li, li_gao82@yeah.net

https://doi.org/10.26599/POM.2026.9140144

Herein, we present the design, synthesis, and investigation of the HER activity of two single-Pt-centered polyoxometalate clusters with an Anderson structure: ligand-free $[PtMo_6(OH)_6O_{18}]^{2-}$ ($PtMo_6$) and ligand-capped $[(PtMo_6(OH)_3O_{18})O_3C_5H_9]^{2-}$ ($PtMo_6$-L). As the electrocatalytically active site, the Pt–O–H moiety is tuned by the capping trimethylolethane ligand, which tailors the electrochemical HER activity of the polyoxometalates. $PtMo_6$-L coated onto glassy carbon exhibits a promising overpotential of 37 mV@10 mA·cm^{-2} (η_{10}) with a Tafel slope of 42 mV·dec^{-1}. Interestingly, naked $PtMo_6$ and $PtMo_6$-L operate via distinct HER pathways (Tafel–Volmer mechanism and Heyrovsky–Volmer mechanism, respectively). Furthermore, $PtMo_6$-L shows good long-term durability. Finally, the HER mechanism over the polyoxometalate clusters is elucidated at the atomic and molecular levels on the basis of experimental and density functional theory (DFT) calculation results.

2 Experimental

2.1 Chemicals

All reagents were of analytical grade and used as received without further purification. Ammonium molybdate tetrahydrate ($(NH_4)_6Mo_7O_{24}\cdot4H_2O$, 99%), chloroplatinic acid ($H_2PtCl_6\cdot6H_2O$, 99%), tetrabutylammonium bromide (TBABr, 98%), and trimethylolethane (H_3-L, 99%) were obtained from Sinopharm Chemical Reagent Corporation. Deionized water was prepared in the laboratory. All glassware was cleaned with aqua regia, rinsed with deionized water, and dried in an oven before use.

2.2 Synthesis of $(PtMo_6(OH)_6O_{18})(NH_4)_2$ ($PtMo_6$) and $[(PtMo_6(OH)_3O_{18})O_3C_5H_9](TBA)_2$ ($PtMo_6$-L)

$PtMo_6$ and $PtMo_6$-L were synthesized using a modified version of a previously reported procedure [32–34]. For $PtMo_6$, typically, 0.75 g of $(NH_4)_6Mo_7O_{24}\cdot4H_2O$ (0.6 mmol) was dissolved in 30 mL of hot water (90 °C), followed by the addition of 36.2 mg of $H_2PtCl_6\cdot6H_2O$ (0.7 mmol), yielding a solution with a pH of 2–3. After 6 h of reaction, the solution was concentrated to ca. 10 mL at 80 °C. Then, the system was allowed to cool to room temperature. After recrystallization from water, the $PtMo_6$ solid was obtained via simple filtration in ~ 51% yield based on the consumption of $H_2PtCl_6\cdot6H_2O$.

$PtMo_6$-L was prepared using $PtMo_6$ as the mother cluster. Typically, $PtMo_6$ was dissolved in 30 mL of hot water (90 °C), and one molar equivalent of H_3-L was added. After 10 h, the system was allowed to cool to room temperature, and TBABr was added. After 1 h, the resulting solids were collected via filtration and thoroughly washed with hot water, affording $PtMo_6$-L in 95% yield based on the consumption of $PtMo_6$. $PtMo_6$-L was recrystallized from water–acetonitrile and used for characterization and electrochemical measurements.

2.3 Characterization

The ultraviolet–visible (UV–vis) spectra of $PtMo_6$ and $PtMo_6$-L in water and acetonitrile, respectively, were recorded on an Agilent Cary 300 spectrophotometer. The electrospray ionization mass spectra (ESI-MS) in the negative mode were obtained using an ion trap mass spectrometer (Thermofisher LTQ, capillary voltage 33 V). Thermogravimetric analysis (TGA) was performed on a Mettler Toledo TGA/SDTA851 instrument under a nitrogen flow with a rate of 20.0 mL·min^{-1} and a heating rate of 10 °C·min^{-1}. Fourier transform infrared (FT-IR) spectra were recorded on a Thermo Fisher Nicolet 6700 instrument in the transmittance mode using a crystal sample mixed with KBr. X-ray photoelectron spectroscopy (XPS) measurements were performed on an X-ray microprobe (ULVAC-PHI Quantera SXM) under an ultrahigh vacuum of 1.0×10^{-7} Torr using an axis HS monochromatized Al Kα cathode source at 150 W, a focused X-ray 100 um beam, a pass energy of 55 eV with a 0.1 eV step length, and a detection angle (take off) of 45°. The binding energy was calibrated with C 1s at 284.8 eV. Inductively coupled plasma-optical emission spectroscopy (ICP-OES) was conducted on an ICP-8100 (Shimadzu) instrument. The ESI-MS of $PtMo_6$ (dissolved in a water–methanol solution (1:1, v/v)) and $PtMo_6$-L (dissolved in acetonitrile) were obtained using a Waters Q-TOF mass spectrometer equipped with a Z-spray source.

2.4 Electrochemical measurements

Electrochemical HER experiments were conducted using a CHI 760C workstation electrolytic cell with a three-electrode system in 0.5 M H_2SO_4 at room temperature. Graphite rod and Ag/AgCl (sat. KCl) electrodes were used as the counter and reference electrodes, respectively. Typically, 5 mg of crystal samples and 40 μL of a 5 wt.% Nafion solution were mixed via ultrasonic treatment for 1 h to form a homogeneous ink. About 6 μL of the above solution was loaded onto glassy carbon (5 mm diameter, loading 0.306 mg·cm^{-2}) to record the linear sweep voltammetry curves at a scan rate of 5 mV·s^{-1}. Long-term stability evaluations were performed via cyclic voltammetry between 0 and −0.3 V (vs. RHE) at a potential sweep rate of 100 mV·s^{-1} for a given number of cycles. For all experiments, the electrocatalyst mass loading kept constant at 0.306 mg·cm^{-2}, and polarization measurements were conducted with 95% *iR* compensation. ICP-OES analysis of Pt species in the electrolyte after the long-term stability tests was performed on an ICP-8100 (Shimadzu) instrument.

2.5 DFT calculations

First-principles calculations were performed using the Vienna *ab initio* simulation package [35, 36]. The Perdew–Burke–Ernzerhof functional within the generalized-gradient approximation was adopted for electron exchange-correlation [37]. The projector-augmented-wave method [38] was employed to characterize electron–ion interactions using a kinetic energy cutoff of 520 eV to model the valence electron density. A Γ-centered k-point mesh of $2 \times 2 \times 1$ was used for geometric optimization, and a denser $5 \times 5 \times 1$ mesh was used for electronic structure calculations to sample the Brillouin zone. Convergence criteria were set to 10^{-5} eV for the total energy and 0.05 eV·Å^{-1} for atomic forces. In accordance with the corresponding crystal structures, $PtMo_6$ and $PtMo_6$-L clusters were separated by a 15 Å vacuum. The Gibbs free-energy change for hydrogen adsorption (ΔG_{H^*}) was obtained using the formula $\Delta G_{H^*} = \Delta E_{H^*} + \Delta E_{ZPE} - T\Delta S$, where ΔE_{H^*}, ΔE_{ZPE}, ΔS, and T are the adsorption energy of hydrogen, the change in zero-point energy, the entropy change associated with hydrogen adsorption, and the temperature (298.15 K), respectively.

3 Results and discussion

3.1 Synthesis and characterization of $PtMo_6$ and $PtMo_6$-L

The single-Pt-centered Anderson-typed polyoxometalate cluster

$PtMo_6$ was prepared via a modified previously reported method [32–34]. $PtMo_6$-L was obtained by directly grafting a trimethylolethane ligand on one side of the $PtMo_6$ molecule using a post-synthesis modification method. Both clusters were purified via recrystallization before characterization.

UV–vis spectroscopy, a straightforward and effective tool for evaluating the charge transfer in materials, was used to determine the structures of $PtMo_6$ in water and $PtMo_6$-L in acetonitrile. As presented in Fig. 1(a), the characteristic absorption bands of $PtMo_6$ and $PtMo_6$-L appear at 375 and 364 nm, respectively, indicating that the absorption underwent a slight blueshift after grafting the trimethylolethane ligand. These bands can be attributed to the $^1A_{lg} \rightarrow {}^1T_{lg}$ transitions of the octahedral [PtO_6] moiety in $PtMo_6$ and $PtMo_6$-L, suggesting that single-atom Pt is located at the center of the clusters. In addition, the absorption band at 426 nm for $PtMo_6$-L is attributable to $^1A_{lg} \rightarrow {}^3T_{lg}$ transitions [39], demonstrating the successful incorporation of the L ligand on the $PtMo_6$ surface. The UV–vis results suggest that $PtMo_6$ and $PtMo_6$-L exhibit a similar topological structure to that of our previously reported $CuMo_6$-based Anderson-type polyoxometalate [40].

Next, the chemical formula and purity of $PtMo_6$ and $PtMo_6$-L were studied using ICP-MS and ESI-MS [41]. Using $PtMo_6$ and $PtMo_6$-L samples dissolved in aqua regia, the Mo/Pt molar ratios were determined to be 6.1 for $PtMo_6$ and 5.9 for $PtMo_6$-L via ICP-MS. Meanwhile, the ESI-MS analysis was conducted using water solutions of the clusters to preserve their molecular structures. No signals were found in the mass range of 100–1000 Da in the positive mode, implying that $PtMo_6$ and $PtMo_6$-L are negatively charged, as most polyoxometalates. In the negative mode, prominent ESI-MS peaks were detected in the range of *m/z* 575–587 Da for $PtMo_6$ (Fig. 1(b)) and *m/z* 606–622 Da for $PtMo_6$-L (Fig. 1(c)). The spacing of the experimental isotopic patterns was 0.5 Da (0.5 = 1/2) in both cases, indicating that the charge of the $PtMo_6$ and $PtMo_6$-L anions is −2. Specifically, the distinct mass peak at *m/z* 580.38 Da in Fig. 1(b) can be assigned to the $[PtMo_6(OH)_6O_{18}]^{2-}$ anion ($PtMo_6O_{24}H_6$, theoretical *m/z* (*z* = 2): 508.37 Da), and the sharp mass peak at *m/z* 614.64 Da in Fig. 1(c) can be assigned to the $[(PtMo_6(OH)_3O_{18})O_3C_5H_9]^{2-}$ anion ($PtMo_6O_{24}C_5H_{12}$, theoretical *m/z* (*z* = 2): 613.43 Da), confirming the successful introduction of the L ligand on the $PtMo_6$ molecule, consistent with the UV–vis spectroscopy analysis.

Single-crystal X-ray diffraction (SCXRD) was used to determine the atomically precise structure of $PtMo_6$ and $PtMo_6$-L. The SCXRD results revealed that the $PtMo_6$ motif has a flat Anderson topology (α type), with six edge-sharing MoO_6 octahedra surrounding a central PtO_6 unit (Fig. 2(a)). The length of the terminal Mo–O bond is 1.719(3) Å, and that of the lateral bridging Mo–O bond is 1.912(2)–1.953(3) Å. Six μ_3-O atoms bind with six protons on each side of $PtMo_6$, where the Pt–O and Mo–O bond lengths are 1.971(2)–1.984(3) and 2.262(3)–2.320(3) Å, respectively. The distance between the Pt center and Mo is 3.310(2) Å. This structure is similar to that reported by Lee's group [42].

Unfortunately, no single crystals of $PtMo_6$-L could be obtained. Nevertheless, comparison of the UV–vis and mass spectra of $PtMo_6$ and $PtMo_6$-L indicates that $PtMo_6$-L contains one trimethylolethane ligand anchored on $PtMo_6$ via three μ_3-O atoms on one side, replacing three surface protons in $PtMo_6$ (Fig. 2(b)). The remaining μ_3-O atoms are still coordinated with three protons (Fig. 2(b)). Meanwhile, C–O bonds, Mo=O bonds, and Mo–O–Mo motifs were detected in the FT-IR spectrum of $PtMo_6$-L (Fig. S1 in the Electronic Supplementary Material (ESM)).

To confirm the metal/ligand ratio in $PtMo_6$-L, TGA was conducted in a nitrogen atmosphere. As shown in Fig. 2(c), the TGA curve displays three main stages characterized by weight losses of 5.0 wt.%, 27.8 wt.%, and 9.4 wt.%, corresponding to the removal of adsorbed water, TBA cations (theoretical value: 28.3 wt.%), and trimethylolethane ligand (theoretical value: 9.6 wt.%), respectively. Notably, after the TGA test, the residue was identified as $Pt^{II}Mo^{III}{}_6O_{19}$. This result agrees with the ESI-MS analysis. The chemical environment of Pt in $PtMo_6$-L was further investigated using high-resolution XPS. The binding energy of Pt 4f7/2 in $PtMo_6$-L was 72.2 eV, suggesting that the Pt atom is more positively charged ($Pt^{\delta+}$, $0 < \delta < 2$) than PtO (Pt 4f7/2: 72.8 eV) and metallic Pt^0 (Pt 4f7/2: 71.0 eV) [43].

X-ray absorption spectroscopy was used to elucidate the electronic structure and coordination environment of $PtMo_6$-L using Pt foil and PtO_2 as references (Fig. 3). The extended X-ray absorption fine structure at the Pt L_3 edge revealed the coordination environment of the Pt center. As shown in Fig. 3(a), the Pt L_3-edge (11,568.11 eV) is between those of Pt foil (11,566.27 eV) and PtO_2 (11,568.74 eV), indicating that the chemical state of Pt in $PtMo_6$ is higher than Pt^0 and close to Pt^{4+}. Moreover, no Pt–Pt bond (~ 2.58 Å) was detected in $PtMo_6$-L, indicating the presence of single-atom Pt rather than Pt clusters or particles. Pt–O (2.11 Å) and Pt–Mo (2.90 Å) interactions were observed in $PtMo_6$-L with slight chemical shifts relative to $PtMo_6$ (Fig. 3(b)), consistent with the change in the chemical environment of Pt. These results confirm the high dispersion of individual Pt atoms in $PtMo_6$-L.

3.2 Electrocatalytic performance of $PtMo_6$ and $PtMo_6$-L in the HER

To disclose the effect of the introduced ligand, the electrocatalytic performance of both clusters in the HER was studied in an aqueous 0.5 M H_2SO_4 solution (pH = 0) as the electrolyte, since they are very

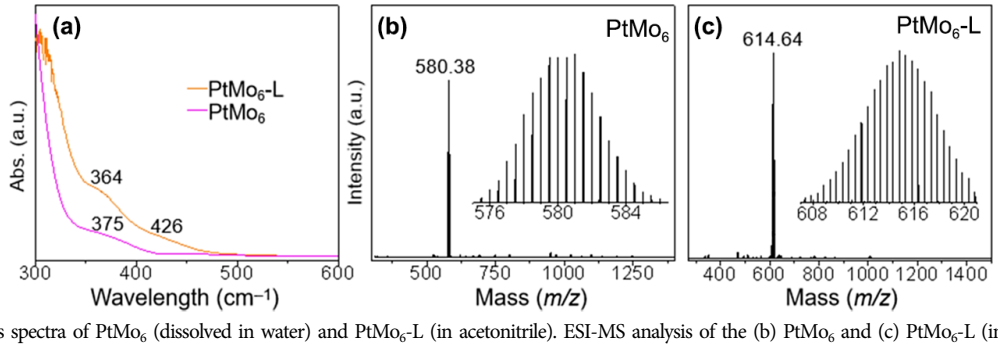


Figure 1 (a) UV–vis spectra of $PtMo_6$ (dissolved in water) and $PtMo_6$-L (in acetonitrile). ESI-MS analysis of the (b) $PtMo_6$ and (c) $PtMo_6$-L (inset: the experimental isotopic distribution patterns; cluster samples were dissolved in water and tested in a negative model).

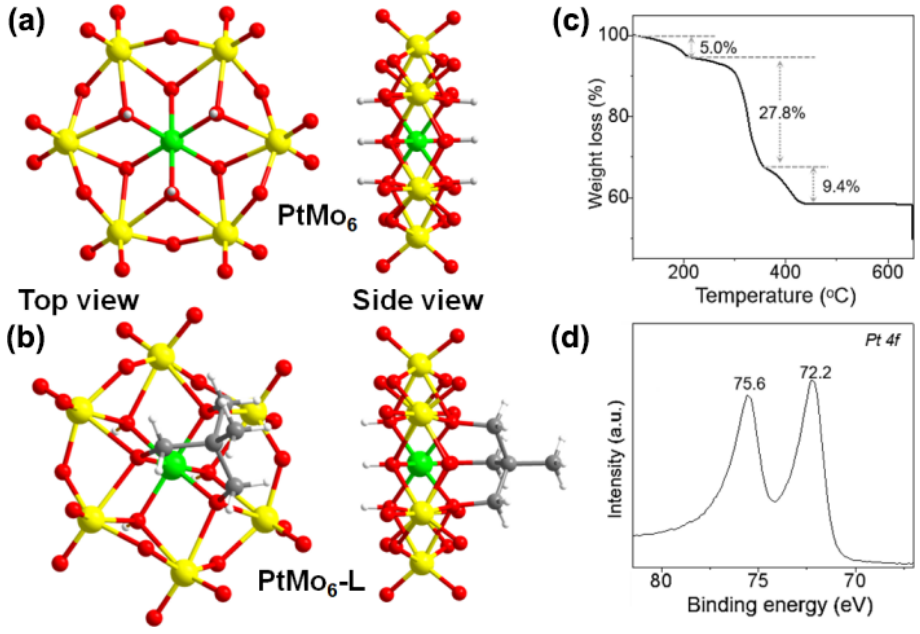


Figure 2 (a) The crystal structure of $PtMo_6$ cluster. (b) The possible structure of $PtMo_6$-L cluster. (Seen from top and side views. Color code: Pt, green; Mo, yellow; O, red; H, white). (c) TGA on $PtMO_6$-L cluster in a N_2 atmosphere. (d) XPS analysis of Pt 4f in $PtMo_6$-L cluster.

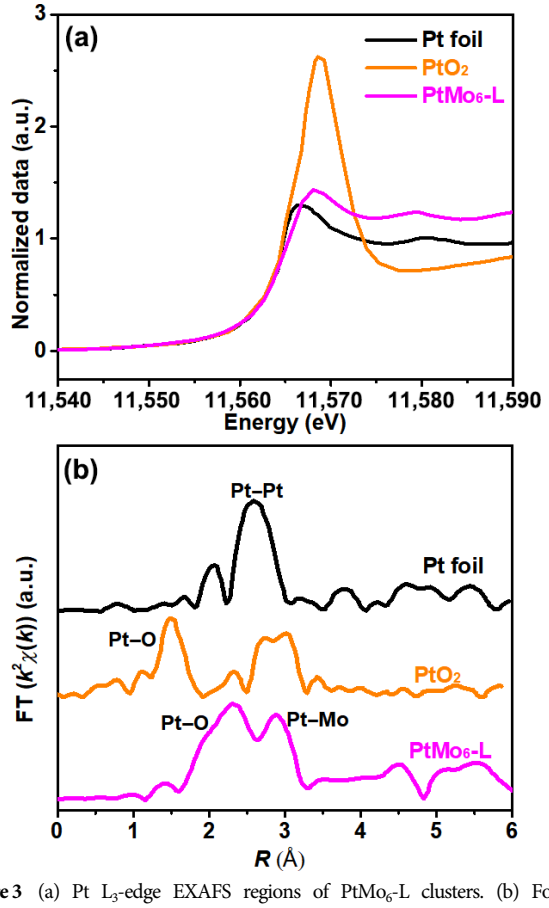


Figure 3 (a) Pt L_3-edge EXAFS regions of $PtMo_6$-L clusters. (b) Fourier-transforms of k^2-weight Pt L_3-edge EXAFS spectra. (Pt foil and PtO_2 are used as references).

stable in acidic solution [44]. The electrocatalytic tests were performed on a standard three-electrode setup with a graphite rod and Ag/AgCl as counter and reference electrodes, respectively, using a commercial 20 wt.% Pt/C electrocatalyst as the reference. The obtained polarization curves are shown in Fig. 4(a). $PtMo_6$-L loaded onto glassy carbon showed a positive overpotential at 10 mA·cm^{-2} (η_{10}) of 37 mV, close to that of commercial Pt/C (η_{10} = 36 mV). Conversely, $PtMo_6$ exhibited poor HER activity (η_{10} = 138 mV), indicating that the electrocatalytic activity is related to the polyoxometalate composition (Fig. 4(b)). Measurements of the mass-normalized HER performance at −0.03 V (Fig. 4(c)) revealed a peak associated with the HER at ~ 132 mA·mg$_{Pt}^{-1}$ for $PtMo_6$-L, which is approximately 8- and 1.5-fold that of $PtMo_6$ (~ 16 mA·mg$_{Pt}^{-1}$) and commercial Pt/C (~ 90 mA·mg$_{Pt}^{-1}$), respectively.

In general, the HER mechanism over the electrocatalyst surface (*) proceeds via the following steps: i) adsorption or Volmer step ($H^+ + e^- + * \rightarrow H^*$); ii) electrochemical desorption or Heyrovsky step ($H^+ + e^- + H^* \rightarrow H_2$); iii) chemical recombination or Tafel step ($2\ H^* \rightarrow H_2$). Generally, Tafel slopes of >110 mV·dec^{-1}, 40–100 mV·dec^{-1}, and < 30 mV·dec^{-1} indicate that the rate-determining step (RDS) is the Tafel step, the Heyrovsky step, and the Volmer step, respectively [45, 46]. Commercial Pt/C showed the lowest Tafel slope of 28 mV·dec^{-1} (Fig. 4(d)), implying that the Volmer step is the RDS. Meanwhile, $PtMo_6$-L exhibited a Tafel slope of 42 mV·dec^{-1}, indicating that the RDS is the Heyrovsky step. Thus, both Pt/C and $PtMo_6$-L electrocatalysts most likely obey the Heyrovsky–Volmer mechanism. In contrast, the Tafel slope of naked $PtMo_6$ was the highest (103 mV·dec^{-1}), meaning that the Tafel step is the RDS and this electrocatalyst operates via the Tafel–Volmer mechanism. These results demonstrate that the TBA surface ligand affects the HER mechanism and RDS of the mononuclear Pt-polyoxometalates.

To further study the HER performance, electrochemical impedance spectroscopy (EIS) measurements were conducted to examine the electrocatalytic kinetics. As shown in Fig. 4(e), the Nyquist plots revealed a smaller semicircle diameter for $PtMo_6$-L than for $PtMO_6$, suggesting a smaller charge transfer resistance in $PtMo_6$-L, which is conducive to the HER activity. The

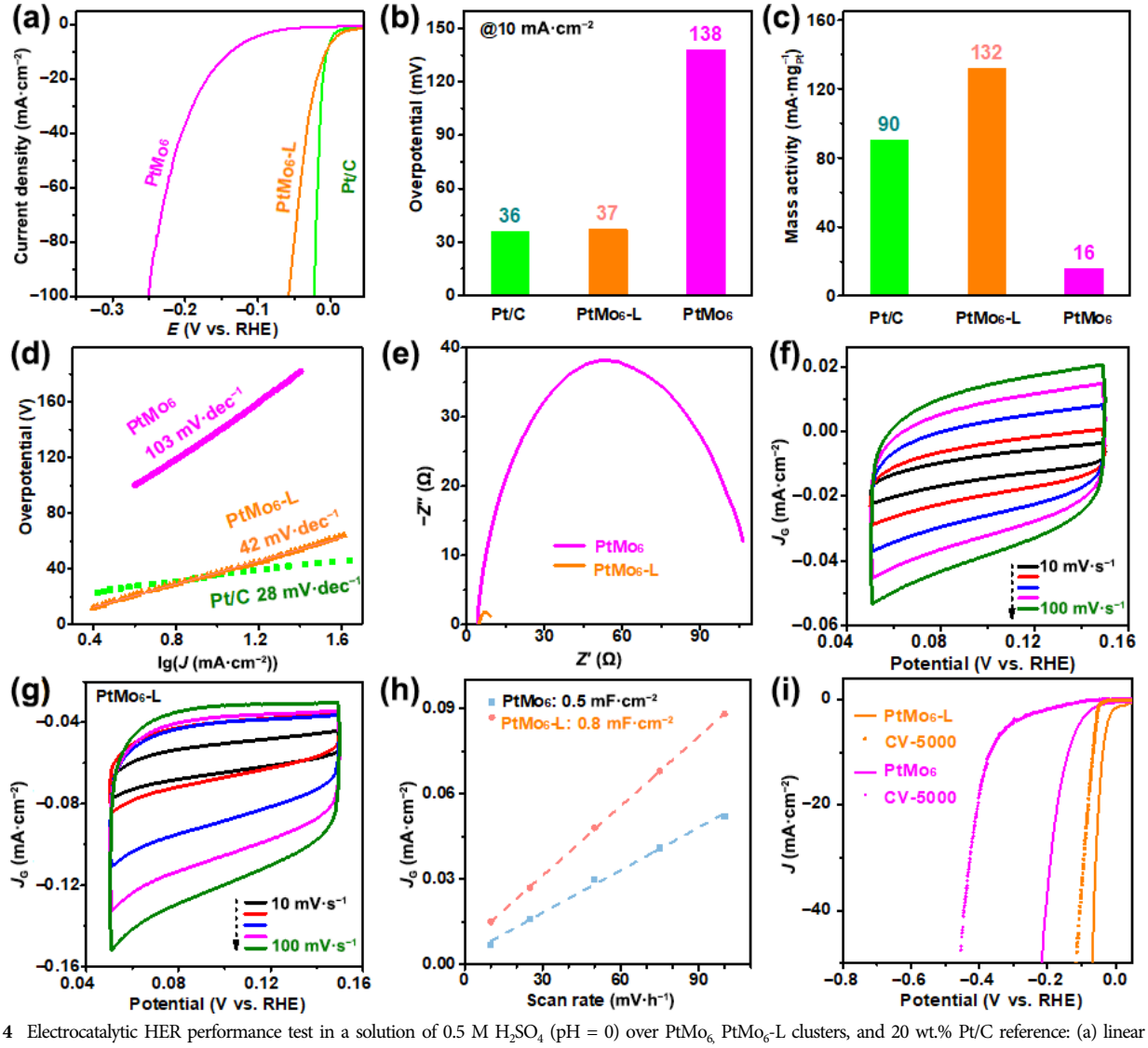


Figure 4 Electrocatalytic HER performance test in a solution of 0.5 M H_2SO_4 (pH = 0) over $PtMo_6$ $PtMo_6$-L clusters, and 20 wt.% Pt/C reference: (a) linear sweep voltammetry curves with 5 mV·s^{-1} and (b) overpotentials at 10 mA·cm^{-2} (η_{10}). (c) Mass activity normalized to the Pt loading at an overpotential of 30 mV. (d) Tafel and (e) Nyquist plots. The double-layer capacitance measurements of (e) $PtMo_6$ and (f) $PtMo_6$-L clusters. (g) Capacitive currents at different scan rates. (i) Long-term durability measurements for 5000 CV cycles.

electrochemical double-layer capacitance of $PtMo_6$-L (0.8 mF·cm^{-2}) was larger than that of $PtMO_6$ (0.5 mF·cm^{-2}), suggesting a much greater electrochemically active surface area (Figs. 4(f)–4(h)). The observed electrocatalytic activities and EIS results are consistent with $PtMo_6$ exhibiting a nanosized metal oxide structure. The electrocatalytic results demonstrate that the $PtMo_6$-L electrocatalyst exhibits high HER activity owing to the favorable reaction kinetics stemming from the enhanced mass and charge transport.

Furthermore, the clusters were subjected to long-term durability measurements over the voltage range of 0 to −0.5 V (vs. RHE) at a scan rate of 100 mV·s^{-1}. As shown in Fig. 4(i) (orange profiles), $PtMo_6$-L exhibited an excellent stability, with only a slight decline in activity from the initial η_{10} of 37 to 66 mV after 5000 cycles. This activity degradation can be attributed to the slow etching of $PtMo_6$-L in acidic solution or ligand loss. Conversely, the HER activity of $PtMo_6$ decreased from the initial η_{10} of 138 to 367 mV after 5000 cycles, which is also caused by partial detachment of $PtMo_6$ clusters in the acidic solution. This is consistent with the results of the ICP-OES analysis of the electrolytes after the long-term durability tests, which revealed that the amount of Pt cations increased from the initial value of 287 to 1966 ppm. Moreover, the robustness of $PtMo_6$ and $PtMo_6$-L was further evaluated using the current–time curves. As shown in Fig. S2 in the ESM, $PtMo_6$-L was much more robust than $PtMo_6$ owing to the grafted TBA ligand. In addition, the UV–vis spectrum of $PtMo_6$-L remained unaltered after a 12 h test (Fig. S3 in the ESM), indicating that the initial structure of $PtMo_6$-L was preserved, which can also be attributed to the grafted TBA ligand. The difference in HER performance between the two clusters ($PtMo_6$ and $PtMo_6$-L, Fig. 4(a)) most likely stems from the unique textural and electronic structures of the single-Pt-centered polyoxometalates.

3.3 Mechanism investigation

Finally, DFT calculations were performed to elucidate the role of the Pt–O–H moieties in the HER [8]. Structural optimization was conducted on the $PtMo_6$ and $PtMo_6$-L surfaces, finding four types of O atoms, which are sequentially numbered in Fig. 5(a). In detail, Pt atoms form a six-coordinated octahedral structure with O atoms,

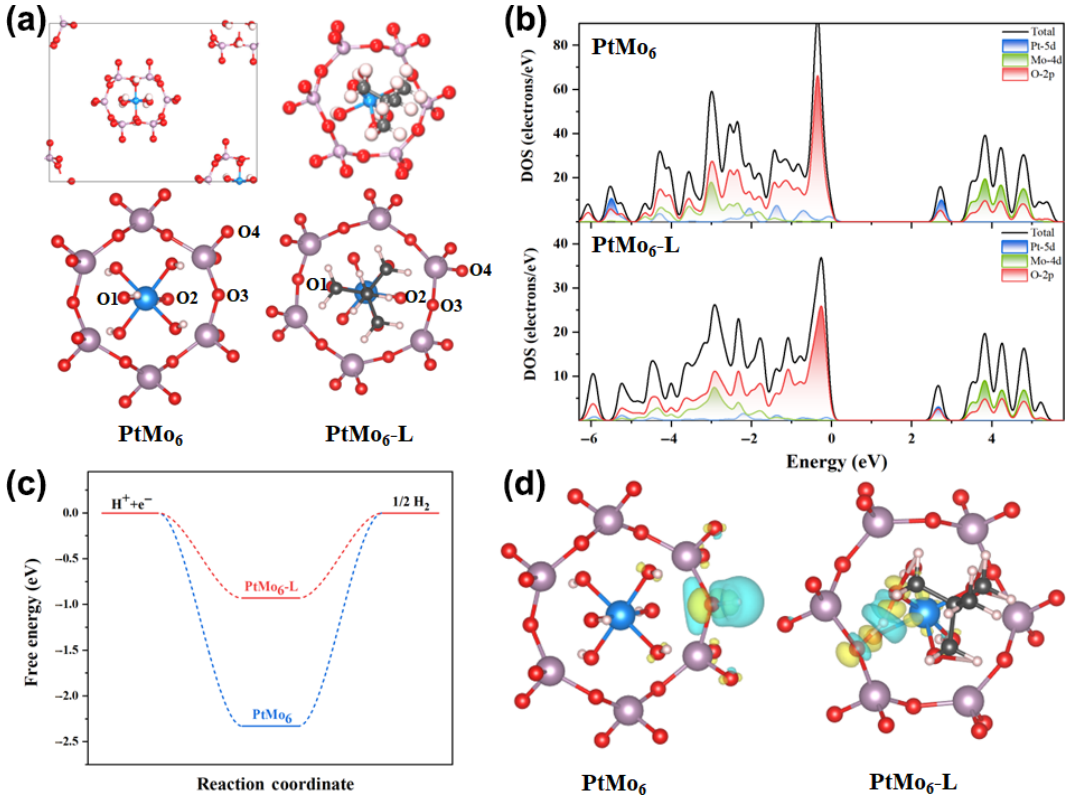


Figure 5 (a) DFT simulated structures of $PtMo_6$ and $PtMo_6$-L. (b) Density of states (DOS) plots, (c) free energy profiles of hydrogen evolution reaction, and (d) electron density difference distribution diagrams around active spots over $PtMo_6$ and $PtMo_6$-L. (Part of O–Mo bonds in $PtMo_6$ and $PtMo_6$-L were omitted for highlight H atoms).

whereas Mo atoms adopt a four-coordinated regular tetrahedral configuration with O atoms. The Pt–O1, Pt–O2, Mo–O3, and Mo–O4 bond lengths in $PtMo_6$ were 2.01, 2.01, 1.94, and 1.73 Å, respectively. In $PtMo_6$-L, the Pt–O1 bond length was marginally shorter (1.99 Å), and the remaining bond lengths were comparable to those in $PtMo_6$, consistent with the SCXRD results. This indicates that the interaction between Pt and the O1 atom was reinforced by the incorporation of the C_5H_9 ligand. Accordingly, the density of states results revealed that the Pt-5d and O-2p orbitals of $PtMo_6$-L were more delocalized near the Fermi level compared with those of $PtMo_6$ (Fig. 5(b)). Bader charge calculations indicated that, compared with the corresponding O1 atom in $PtMo_6$, the C_5H_9-bonded O1 in $PtMo_6$-L possessed a more negative charge of −1.43 e.

ΔG_{H^*} is an important descriptor for evaluating the HER electrocatalytic activity. Weak hydrogen–surface interactions lead to adsorption being the RDS for electrocatalysis, whereas the strong interaction will increase the difficulty of the desorption process. For an electrocatalyst to exhibit optimal HER performance, its ΔG_{H^*} should approach zero. As shown in Fig. 5(c), $PtMo_6$-L showed a ΔG_{H^*} of −0.93 eV, which is closer to 0 eV than that of $PtMo_6$ (ΔG_{H^*} = −2.33 eV), revealing the underlying reason for the enhanced HER electrocatalytic performance of $PtMo_6$-L. In addition, $PtMo_6$ and $PtMo_6$-L exhibited distinct proton adsorption sites (Fig. 5(d)). In $PtMo_6$, protons preferentially bind to O3 owing to its higher charge density relative to that of O4, rendering it the favorable proton adsorption site. In contrast, in $PtMo_6$-L, protons are located in the interstitial space between O1 and O3.

According to the experimental and DFT calculation results, the following pathway can be proposed for the acidic HER over $PtMo_6$ and $PtMo_6$-L. For $PtMo_6$, the protons are selectively adsorbed on the O1 atom, which is reduced by electrons on the electrode surface. Then, two adsorbed H atoms (H*) combine with each other and detach from the electrocatalyst surface to form one free hydrogen molecule, following the Tafel–Volmer pathway (Fig. 6(a)). In contrast, protons are adsorbed on the interstitial space between O1 and O3 in $PtMo_6$-L and then reduced by electrons to give H* species, which further react with another proton and an electron to produce a hydrogen molecule. Thus, the Heyrovsky–Volmer pathway is favored over $PtMo_6$-L (Fig. 6(b)). Overall, the results demonstrate that surface ligand engineering of mononuclear Pt-polyoxometalates modifies their electronic structures and, in turn, their electrocatalytic behavior.

4 Conclusions

Two single-Pt-centered polyoxometalate clusters, $PtMo_6$ and $PtMo_6$-L, were prepared and characterized. Both clusters share similar geometric structures except for the introduced ligand, which plays a

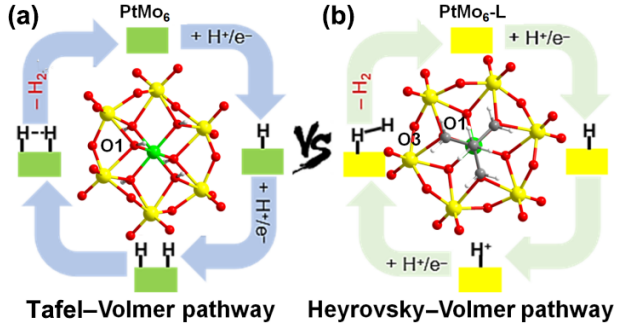


Figure 6 The tentative HER mechanism over (a) $PtMo_6$ and (b) $PtMo_6$-L clusters.

key role in the HER performance. Pt_1Mo_6-L exhibits excellent electrocatalytic activity comparable to that of commercial 20 wt.% Pt/C, with an overpotential of 37 mV@10 mA·cm^{-2} and a mass activity of 132 mA·mg^{-1}. Furthermore, $PtMo_6$-L exhibits good long-term stability, with a small Tafel slope of 42 mV·dec^{-1}. Interestingly, the surface ligand tailors the HER mechanism: The HER over naked $PtMo_6$ follows the Tafel–Volmer mechanism, whereas $PtMo_6$-L operates via the Heyrovsky–Volmer mechanism, similar to commercial Pt/C. The Pt–O–H group plays an important role in the electrocatalytic HER, as confirmed by DFT calculations. This study provides new insights into the electrocatalytic activity of polyoxometalate clusters at the precise atomic and molecular levels.

Electronic Supplementary Material: Supplementary material (FT-IR and UV–vis spectra, mass activity, crystal data and structure refinement for $PtMo_6$, and bader charges of Pt atoms) is available in the online version of this article at https://doi.org/10.26599/POM.2026.9140144.

Data availability

All data needed to support the conclusions in the paper are presented in the manuscript. Additional data related to this paper may be requested from the corresponding author upon request.

Acknowledgements

This work is granted by Science and Technology Plan Joint Program of Liaoning Province (Natural Science Foundation for General Project) (No. 2025-MSLH-623).

Declaration of competing interest

All authors report no conflict of interest in this work.

Author contribution statement

Z. X. Q.: Methodology, investigation, writing – original draft, supervision, formal analysis. H. L.: Methodology, investigation, formal analysis. C. L. C.: Visualization. W. J.: DFT, conceptualization, writing – review & editing. J. J. Z.: Visualization. G. L.: Writing – review & editing, supervision, project administration, conceptualization.

Use of AI statement

None.

References

[1] Zhu, Y. L.; Tahini, H. A.; Hu, Z. W.; Dai, J.; Chen, Y. B.; Sun, H. N.; Zhou, W.; Liu, M. L.; Smith, S. C.; Wang, H. T. et al. Unusual synergistic effect in layered Ruddlesden-Popper oxide enables ultrafast hydrogen evolution. *Nat. Commun.* **2019**, *10*, 149.

[2] Ahmad, I.; Li, H.; Ahmed, S. B.; Alotaibi, M. T.; Li, G. Shedding light on unprecedented spatial confinement of metal clusters by metal/covalent organic frameworks for photocatalysis. *Appl. Phys. Rev.* **2025**, *12*, 041327.

[3] Sanwal, P.; Zhang, J. J.; Wang, H. D.; Babar, Z. U. D.; Zhang, Y. F.; Peng, X. J.; Li, G. Simultaneous activity and stability gains in PEM electrolyzer via targeted Cr^{3+} occupation in spinel Co_3O_4 octahedral lattices. *Nano Res.* **2026**, *19*, 94908133.

[4] Hossain, M. D.; Liu, Z. J.; Zhuang, M. H.; Yan, X. X.; Xu, G. L.; Gadre, C. A.; Tyagi, A.; Abidi, I. H.; Sun, C. J.; Wong, H. et al. Rational design of graphene-supported single atom catalysts for hydrogen evolution reaction. *Adv. Energy Mater.* **2019**, *9*, 1803689.

[5] Chen, W. X.; Pei, J. J.; He, C. T.; Wan, J. W.; Ren, H. L.; Wang, Y.; Dong, J. C.; Wu, K. L.; Cheong, W. C.; Mao, J. J. et al. Single tungsten atoms supported on MOF-derived n-doped carbon for robust electrochemical hydrogen evolution. *Adv. Mater.* **2018**, *30*, 1800396.

[6] Huang, J.; Tian, M.; Tong, L.; Zhu, L. H.; Li, L. L.; Liao, X. P.; Gao, Q. S.; Wang, W. Z.; Yang, Z. Q.; Liang, T. X. et al. Synergism of tiny Ni clusters and Pt nanoparticles promoting efficient and stable electrocatalytic methanol oxidation and hydrogen evolution by water electrolysis. *Green Chem.* **2025**, *27*, 6619–6629.

[7] Pei, A.; Li, G.; Zhu, L. H.; Huang, Z. N.; Ye, J. Y.; Chang, Y. C.; Osman, S. M.; Pao, C. W.; Gao, Q. S.; Chen, B. H. et al. Nickel hydroxide-supported Ru single atoms and Pd nanoclusters for enhanced electrocatalytic hydrogen evolution and ethanol oxidation. *Adv. Funct. Mater.* **2022**, *32*, 2208587.

[8] Liu, C. G.; Jiang, M. X.; Su, Z. M. Computational study on M_1/POM single-atom catalysts (M = Cu, Zn, Ag, and Au; POM = $[PW_{12}O_{40}]^{3-}$): Metal-support interactions and catalytic cycle for alkene epoxidation. *Inorg. Chem.* **2017**, *56*, 10496–10504.

[9] Zhang, B.; Asakura, H.; Zhang, J.; Zhang, J. G.; De, S.; Yan, N. Stabilizing a $Platinum_1$ single-atom catalyst on supported phosphomolybdic acid without compromising hydrogenation activity. *Angew. Chem., Int. Ed.* **2016**, *55*, 8319–8323.

[10] Lin, L. L.; Zhou, W.; Gao, R.; Yao, S. Y.; Zhang, X.; Xu, W. Q.; Zheng, S. J.; Jiang, Z.; Yu, Q. L.; Li, Y. W. et al. Low-temperature hydrogen production from water and methanol using Pt/α-MoC catalysts. *Nature* **2017**, *544*, 80–83.

[11] Cheng, N. C.; Stambula, S.; Wang, D.; Banis, M. N.; Liu, J.; Riese, A.; Xiao, B. W.; Li, R. Y.; Sham, T. K.; Liu, L. M. et al. Platinum single-atom and cluster catalysis of the hydrogen evolution reaction. *Nat. Commun.* **2016**, *7*, 13638.

[12] Tiwari, J. N.; Sultan, S.; Myung, C. W.; Yoon, T.; Li, N. N.; Ha, M. R.; Harzandi, A. M.; Park, H. J.; Kim, D. Y.; Chandrasekaran, S. S. et al. Multicomponent electrocatalyst with ultralow Pt loading and high hydrogen evolution activity. *Nat. Energy* **2018**, *3*, 773–782.

[13] Yin, X. P. Wang, H. J.; Tang, S. F.; Lu, X. L.; Shu, M.; Si, R.; Lu, T. B. Engineering the coordination environment of single-atom platinum anchored on graphdiyne for optimizing electrocatalytic hydrogen evolution. *Angew. Chem., Int. Ed.* **2018**, *57*, 9382–9386.

[14] Pei, A.; Xie, R. K.; Zhu, L. H.; Wu, F. S.; Huang, Z. N.; Pang, Y. Y.; Chang, Y. C.; Chai, G. L.; Pao, C. W.; Gao, Q. S. et al. Methanol-enhanced low-cell-voltage hydrogen generation at industrial-grade current density by triadic active sites of Pt_1–Pd_n-$(Ni,Co)(OH)_x$. *J. Am. Chem. Soc.* **2025**, *147*, 3185–3194.

[15] Pei, A.; Xie, R. K.; Zhang, Y.; Feng, Y. L.; Wang, W. Z.; Zhang, S. F.; Huang, Z. N.; Zhu, L. H.; Chai, G. L.; Yang, Z. Q. et al. Effective electronic tuning of Pt single atoms *via* heterogeneous atomic coordination of $(Co,Ni)(OH)_2$ for efficient hydrogen evolution. *Energy Environ. Sci.* **2023**, *16*, 1035–1048.

[16] Liu, L. L.; Wang, L.; Xiao, X. Y.; Yang, P.; Zhao, J. W.; Kortz, U. Structural overview and evolution paths of lacunary polyoxometalates. *Coord. Chem. Rev.* **2024**, *506*, 215687.

[17] Nyman, M.; Burns, P. C. A comprehensive comparison of transition-metal and actinyl polyoxometalates. *Chem. Soc. Rev.* **2012**, *41*, 7354–7367.

[18] Ahmad, I.; Li, H.; Al-Qattan, A.; Alotaibi, M. T.; Li, G. Metal cluster confinement in MOFs and COFs: Advanced synthesis strategies and applications in photocatalysis. *Polyoxometalates* **2026**, *5*, 9140122.

[19] Izarova, N. V.; Pope, M. T.; Kortz, U. Noble metals in polyoxometalates. *Angew. Chem., Int. Ed.* **2012**, *51*, 9492–9510.

[20] Blasco-Ahicart, M.; Soriano-López, J.; Carbó, J. J.; Poblet, J. M.; Galan-Mascaros, J. R. Polyoxometalate electrocatalysts based on earth-abundant metals for efficient water oxidation in acidic media. *Nat. Chem.* **2018**, *10*, 24–30.

[21] Liu, R. J.; Zhang, G. J.; Cao, H. B.; Zhang, S. J.; Xie, Y. B.; Haider, A.; Kortz, U.; Chen, B. H.; Dalal, N. S.; Zhao, Y. S. et al. Enhanced proton and electron reservoir abilities of polyoxometalate grafted on graphene for high-performance hydrogen evolution. *Energy Environ. Sci.* **2016**, *9*, 1012–1023.

[22] Chen, J. J.; Symes, M. D.; Cronin, L. Highly reduced and protonated aqueous solutions of $[P_2W_{18}O_{62}]^{6-}$ for on-demand hydrogen generation and energy storage. *Nat. Chem.* **2018**, *10*, 1042–1047.

[23] Zhang, J. J.; Guo, S.; Li, T. Z.; Zhang, Y. F.; Zeng, Q.; Sanwal, P.; Xu, L. L.; Li, G. Unravelling the high-valence iridium single-atoms on $MnCoO_x$ clusters for proton exchange membrane water electrolyzer. *Appl. Catal. B: Environ. Energy* **2025**, *377*, 125518.

[24] Zhang, B.; Sun, G.; Ding, S. P.; Asakura, H.; Zhang, J.; Sautet, P.; Yan, N. Atomically dispersed Pt_1-polyoxometalate catalysts: How does metal-support interaction affect stability and hydrogenation activity? *J. Am. Chem. Soc.* **2019**, *141*, 8185–8197.

[25] Zhang, J. W.; Huang, Y. C.; Li, G.; Wei, Y. G. Recent advances in alkoxylation chemistry of polyoxometalates: From synthetic strategies, structural overviews to functional applications. *Coord. Chem. Rev.* **2019**, *378*, 395–414.

[26] Wang, S. S.; Yang, G. Y. Recent advances in polyoxometalate-catalyzed reactions. *Chem. Rev.* **2015**, *115*, 4893–4962.

[27] Paille, G.; Gomez-Mingot, M.; Roch-Marchal, C.; Lassalle-Kaiser, B.; Mialane, P.; Fontecave, M.; Mellot-Draznieks, C.; Dolbecq, A. A fully noble metal-free photosystem based on cobalt-polyoxometalates immobilized in a porphyrinic metal-organic framework for water oxidation. *J. Am. Chem. Soc.* **2018**, *140*, 3613–3618.

[28] Copéret, C.; Comas-Vives, A.; Conley, M. P.; Estes, D. P.; Fedorov, A.; Mougel, V.; Nagae, H.; Núñez-Zarur, F.; Zhizhko, P. A. Surface organometallic and coordination chemistry toward single-site heterogeneous catalysts: Strategies, methods, structures, and activities. *Chem. Rev.* **2016**, *116*, 323–421.

[29] Tanielyan, S. K.; Augustine, R. L.; Marin, N.; Alvez, G. Anchored Wilkinson catalyst. *ACS Catal.* **2011**, *1*, 159–169.

[30] He, P. L.; Xu, B.; Xu, X. B.; Song, L.; Wang, X. Surfactant encapsulated palladium-polyoxometalates: Controlled assembly and their application as single-atom catalysts. *Chem. Sci.* **2016**, *7*, 1011–1015.

[31] Yu, F. Y.; Lang, Z. L.; Yin, L. Y.; Feng, K.; Xia, Y. J.; Tan, H. Q.; Zhu, H. T.; Zhong, J.; Kang, Z. H.; Li, Y. G. Pt–O bond as an active site superior to Pt^0 in hydrogen evolution reaction. *Nat. Commun.* **2020**, *11*, 490.

[32] Chen, Y. D.; Tian, S. L.; Qin, Z. X.; Zhang, J. W.; Cao, Y. H.; Chu, S. Q.; Lu, L. L.; Li, G. $[MW_{12}O_{44}]$ clusters: Unprecedented central heteroatoms atomically dispersed in the eight coordination state bridging the 1:12 polyoxometalate family of Keggin and Silverton. *Nanoscale* **2019**, *11*, 22270–22276.

[33] Chen, Y. D.; Zhang, C. L.; Yang, C. P.; Zhang, J. W.; Zheng, K.; Fang, Q. H.; Li, G. A Waugh type $[CoMo_9O_{32}]^{6-}$ cluster with atomically dispersed Co^{IV} originates from Anderson type $[CoMo_6O_{24}]^{3-}$ for photocatalytic oxygen molecule activation. *Nanoscale* **2017**, *9*, 15332–15339.

[34] Peacock, R. D.; Weakley, T. J. R. Heteropolytungstate complexes of the lanthanide elements. Part I. Preparation and reactions. *J. Chem. Soc. A* **1971**, *6*, 1836–1839.

[35] Kresse, G.; Furthmüller, J. Efficiency of *ab-initio* total energy calculations for metals and semiconductors using a plane-wave basis set. *Comput. Mater. Sci.* **1996**, *6*, 15–50.

[36] Kresse, G.; Furthmuller, J. Efficient iterative schemes for *ab initio* total-energy calculations using a plane-wave basis set. *Phys. Rev. B* **1996**, *54*, 11169–11186.

[37] Perdew, J. P.; Burke, K.; Ernzerhof, M. Generalized gradient approximation made simple [Phys. Rev. Lett. 77, 3865 (1996)]. *Phys. Rev. Lett.* **1997**, *78*, 1396.

[38] Kresse, G.; Joubert, D. From ultrasoft pseudopotentials to the projector augmented-wave method. *Phys. Rev. B* **1999**, *59*, 1758–1775.

[39] Jin, Z. S.; Chen, Z. S.; Li, Q. L.; Xi, C. J.; Zheng, X. H. On the conditions and mechanism of PtO_2 formation in the photoinduced conversion of H_2PtCl_6. *J. Photochem. Photobiol. A* **1994**, *81*, 177–182.

[40] Fang, Q. H.; Fu, J. H.; Wang, F.; Qin, Z. X.; Ma, W. G.; Zhang, J. W.; Li, G. Tris functionalized Cu-centered cyclohexamolybdate molecular armor as a bimetallic catalyst for rapid p-nitrophenol hydrogenation. *New J. Chem.* **2019**, *43*, 28–36.

[41] Gu, X. R.; Guo, S.; Zhang, Y. F.; Zhang, J. J.; Sanwal, P.; Xu, L. L.; Zhao, Z.; Jin, R. C.; Li, G. Boosting oxygen evolution performance over synergistic tiara nickel clusters and thin layered double hydroxides. *Nano Res. Energy* **2024**, *3*, e9120134.

[42] Joo, H. C.; Park, K. M.; Lee, U. Crystal structure of undecapotassium bis[α-hemipentahydrogen hexamolybdoplatinate(IV)] dodecahydrate. *Acta Crystallogr. E Crystallogr. Commun.* **2015**, *71*, 986–988.

[43] Biesinger, M. C.; Payne, B. P.; Grosvenor, A. P.; Lau, L. W. M.; Gerson, A. R.; Smart, R. S. C. Resolving surface chemical states in XPS analysis of first row transition metals, oxides and hydroxides: Cr, Mn, Fe, Co and Ni. *Appl. Surf. Sci.* **2011**, *257*, 2717–2730.

[44] Gu, X. R.; Zhang, J. J.; Guo, S.; Zhang, Y. F.; Xu, L. L.; Jin, R. C.; Li, G. Tiara Ni clusters for electrocatalytic nitrate reduction to ammonia with 97% faradaic efficiency. *J. Am. Chem. Soc.* **2025**, *147*, 22785–22795.

[45] Doyle, R. L.; Godwin, I. J.; Brandon, M. P.; Lyons, M. E. G. Redox and electrochemical water splitting catalytic properties of hydrated metal oxide modified electrodes. *Phys. Chem. Chem. Phys.* **2013**, *15*, 13737.

[46] Sanwal, P.; Raza, A.; Miao, Y. X.; Lumbers, B.; Li, G. Advances in coinage metal nanoclusters: From synthesis strategies to electrocatalytic performance. *Polyoxometalates* **2024**, *3*, 9140057.



Gao Li, professor (doctorial tutor), received his BSc (2004) from Hunan Normal University and PhD (2011) from Shanghai Jiaotong University. After the research in Carnegie Mellon University (USA, 2011–2014) and Dalian Institute of Chemical Physics, Chinese Academy of Science (2014–2025), he joined Inner Mongolia Normal University. His current research interests focused on the preparation and application of small-sized particle catalysts, e.g. noble metal clusters and metal oxides. His bibliography includes over 250 publications.

Open Access This article is licensed under the terms of the Creative Commons Attribution 4.0 International License (http://creativecommons.org/licenses/by/4.0/), which permits use, sharing, distribution and reproduction in any medium, provided the original work is properly cited.

© The author(s) 2026. Published by Tsinghua University Press.